

**The Mass–Luminosity Relation in the L/T Transition:  
Individual Dynamical Masses for the New *J*-Band Flux Reversal Binary  
SDSS J105213.51+442255.7AB<sup>\*,†</sup>**

Trent J. Dupuy,<sup>1</sup> Michael C. Liu,<sup>2</sup> S. K. Leggett,<sup>3</sup> Michael J. Ireland,<sup>4</sup> Kuenley Chiu,<sup>5</sup>  
and David A. Golimowski<sup>6</sup>

**ABSTRACT**

We have discovered that SDSS J105213.51+442255.7 (T0.5±1.0) is a binary in Keck laser guide star adaptive optics imaging, displaying a large *J*-to-*K*-band flux reversal ( $\Delta J = -0.45 \pm 0.09$  mag,  $\Delta K = 0.52 \pm 0.05$  mag). We determine a total dynamical mass from Keck orbital monitoring ( $88 \pm 5 M_{\text{Jup}}$ ) and a mass ratio by measuring the photocenter orbit from CFHT/WIRCam absolute astrometry ( $M_B/M_A = 0.78 \pm 0.07$ ). Combining these provides the first individual dynamical masses for any field L or T dwarfs,  $49 \pm 3 M_{\text{Jup}}$  for the  $L6.5 \pm 1.5$  primary and  $39 \pm 3 M_{\text{Jup}}$  for the  $T1.5 \pm 1.0$  secondary. Such a low mass ratio for a nearly equal luminosity binary implies a shallow mass–luminosity relation over the L/T transition ( $\Delta \log L_{\text{bol}}/\Delta \log M = 0.6^{+0.6}_{-0.8}$ ). This provides the first observational support that cloud dispersal plays a significant role in the luminosity evolution of substellar objects. Fully cloudy models fail our coevality test for this binary, giving ages for the two components that disagree by 0.2 dex ( $2.0\sigma$ ). In contrast, our observed masses and luminosities can be reproduced at a single age by "hybrid" evolutionary tracks where a smooth change from a cloudy to cloudless photosphere around 1300 K causes slowing of luminosity evolution. Remarkably, such models also match our observed *JHK* flux ratios and colors well. Overall, it seems that the distinguishing features SDSS J1052+4422AB, like a *J*-band flux reversal and high-amplitude variability, are normal for a field L/T binary caught during the process of

---

\*Data presented herein were obtained at the W.M. Keck Observatory, which is operated as a scientific partnership among the California Institute of Technology, the University of California, and the National Aeronautics and Space Administration. The Observatory was made possible by the generous financial support of the W.M. Keck Foundation.

†Based on data obtained with WIRCam, a joint project of CFHT, Taiwan, Korea, Canada, France, at the Canada-France-Hawaii Telescope, which is operated by the National Research Council of Canada, the Institut National des Sciences de l'Univers of the Centre National de la Recherche Scientifique of France, and the University of Hawaii.

<sup>1</sup>The University of Texas at Austin, Department of Astronomy, 2515 Speedway C1400, Austin, TX 78712, USA

<sup>2</sup>Institute for Astronomy, University of Hawai'i, 2680 Woodlawn Drive, Honolulu, HI 96822, USA

<sup>3</sup>Gemini Observatory, Northern Operations Center, 670 N. A'ohoku Place, Hilo, HI, 96720 USA

<sup>4</sup>Research School of Astronomy & Astrophysics, Australian National University, Canberra ACT 2611, Australia

<sup>5</sup>C3 Energy, 1300 Seaport Boulevard Suite 500, Redwood City, CA 94063, USA

<sup>6</sup>Space Telescope Science Institute, 3700 San Martin Drive, Baltimore, MD 21218, USA

cloud dispersal, given that the age ( $1.11^{+0.17}_{-0.20}$  Gyr) and surface gravity ( $\log g = 5.0\text{--}5.2$ ) of SDSS J1052+4422AB are typical for field ultracool dwarfs.

*Subject headings:* astrometry — binaries: close — brown dwarfs — parallaxes — stars: fundamental parameters — stars: individual (SDSS J105213.51+442255.7)

## 1. Introduction

Perhaps the most important but uncertain process to model for substellar objects is the formation, growth, and dispersal of condensate clouds. When present in the photosphere, clouds are a dominant opacity source and thereby control basic observable properties like broadband colors, magnitudes, and spectra. In brown dwarfs, clouds appear to grow in influence going from early to late-type L dwarfs then begin dispersing with early-type T dwarfs, resulting in drastic changes in near-infrared spectra. The most prominent features of this transition are that *JHK* colors become significantly bluer (e.g., Leggett et al. 2002) and *J*-band fluxes become brighter (e.g., Dahn et al. 2002) going from late L to early T dwarfs. Early analysis of such observations indicated that the L/T transition occupies a narrow range of effective temperature ( $T_{\text{eff}}$ ), although the underlying physical process explaining the brightening at *J* band was debated. For example, rapid changes in cloud sedimentation efficiency (Knapp et al. 2004) or breakup caused by convection (Burgasser et al. 2002) could reproduce the *J*-band brightening at a single  $T_{\text{eff}}$ , while Tsuji & Nakajima (2003) suggested that mass/age spreads in the population of field brown dwarfs were responsible, not changes in the cloud themselves.

The discovery of binaries at the L/T transition in which one component was directly observed to be brighter at  $1.0\text{--}1.3\ \mu\text{m}$  (*Y* or *J*) but fainter at other wavelengths (*I*, *H*, or *K*; Gizis et al. 2003; Liu et al. 2006) provided the first unambiguous evidence that the *J*-band brightening must occur along a single isochrone. Such flux reversals require a significant flux redistribution as brown dwarfs cool, most likely brought on by changes in cloud opacity. Recent discoveries of large-amplitude variables at near-infrared wavelengths, so far only reliably detected in the L/T transition (e.g., Artigau et al. 2009; Radigan et al. 2012, 2014), support the idea that cloud clearing is spatially heterogeneous in the photosphere. However, without well determined masses and/or ages for any systems that display a *J*-band flux reversal or weather, the alternative possibility of unusual cloud properties, e.g., due to surface gravity, exists. In fact, there still remains only one object in the L/T transition with a precise dynamical mass measurement (LHS 2397aB, photometric spectral type estimate of L7; Dupuy et al. 2009c).

For nearly all substellar objects found to date, evolutionary models are the sole means for estimating their physical properties, typically by using the observed luminosity and an adopted age to yield a model-dependent mass (and temperature, radius, and surface gravity). Such models require an assumption for the photosphere opacity as a boundary condition, and one of the key challenges is the treatment of condensate clouds. The formation, growth, and settling of dust con-

condensates likely occurs at many different levels in the atmosphere and would thus also be influenced both by the local physical conditions and the bulk motions of the gas via convection (Freytag et al. 2010). There are numerous approaches to modeling these complex processes and parameterizing them so that they can be incorporated into one-dimensional atmospheric models (e.g., see recent reviews by Helling & Casewell 2014; Marley & Robinson 2014). However, the currently available evolutionary models assume one of two limiting cases for treatment of the dust. Either dust exists in chemical equilibrium with the gas, resulting in thicker clouds at cooler temperatures (Chabrier et al. 2000), or the grains rapidly fall out of the photosphere as soon as they form, leaving behind dust-free gas (Burrows et al. 1997; Baraffe et al. 2003). Attempting to match the observations described above that dust clouds disperse over a narrow range of  $T_{\text{eff}}$ , Saumon & Marley (2008) computed evolutionary models where the atmosphere is interpolated between the fully cloudy and cloud free limiting cases as objects cool from 1400 K to 1200 K. Despite the limitations of these various simplifying assumptions, current models are at least broadly in accord with the observed substellar sequence in open clusters (e.g., Lodieu et al. 2014; Bouy et al. 2015) and in the field (e.g., Tinney et al. 2003; Saumon & Marley 2008), although discrepancies are obvious in regimes where photospheric condensates play a more significant role, especially the L/T transition.

More stringent test of the theoretical models are now within reach. The past decade saw a growing number of substellar visual binaries with dynamical masses measured via astrometric monitoring (e.g., Lane et al. 2001; Bouy et al. 2004; Liu et al. 2008; Dupuy et al. 2009a,b,c, 2010; Konopacky et al. 2010). The most powerful tests to date come from brown dwarf binaries in a hierarchical triple with a main-sequence star, where the substellar binary orbit gives its dynamical total mass and the primary star gives the system age from gyrochronology. For the two known systems where this is possible, the models seem to predict luminosities that are systematically 0.2–0.4 dex lower than observed (Dupuy et al. 2009b, 2014). However, without individual masses the mass–luminosity relation is unconstrained, and thus a complementary test would be to obtain masses and luminosities for a coeval binary system, even in the absence of an age determination. Previous work has resulted in individual masses for late-M dwarfs, showing broad agreement with the mass–luminosity relation as models approach the substellar boundary.<sup>1</sup> Further tests of evolutionary models are sorely needed, especially in the L/T transition where they are routinely employed to characterize planetary-mass discoveries, e.g., 2MASSW J1207334–393254b (Chauvin et al. 2004), HR 8799bcde (Marois et al. 2008, 2010), and PSO J318.5338–22.8603 (Liu et al. 2013).

We present the discovery of a new  $J$ -band flux reversal binary, SDSS J105213.51+442255.7AB (hereinafter SDSS J1052+4422AB), along with high-precision dynamical masses of the individual components based on resolved orbital monitoring from Keck and absolute astrometry from the

---

<sup>1</sup>Individual masses have been determined for two field late-M dwarf systems: one from resolved radial velocities and relative astrometry (Gl 569Bab; Zapatero Osorio et al. 2004; Simon et al. 2006; Konopacky et al. 2010), and one from absolute astrometry (LHS 1070BC; Seifahrt et al. 2008; Köhler et al. 2012). The young brown dwarf eclipsing binary 2MASS J05352184–0546085AB (M6+M6) in the Orion Nebula Cluster also has well determined individual masses (Stassun et al. 2006).

Canada-France-Hawaii Telescope (CFHT). SDSS J1052+4422 was originally discovered by Chiu et al. (2006). They determined an integrated-light spectral type of  $T0.5 \pm 1.0$  according to the Burgasser et al. (2006) indices ( $T0.0 \pm 1.0$  according to Geballe et al. 2002 indices). More recently, Girardin et al. (2013) found that SDSS J1052+4422 is a high-amplitude variable with peak-to-peak variations of up to 0.06 mag in  $J$  band, although their integrated-light observations could not determine which component was responsible for the variability. Our mass determination for SDSS J1052+4422AB is therefore the first for a  $J$ -band flux reversal binary and the first for a brown dwarf displaying significant weather. More generally, our results are also the first individual mass measurements for any field L or T dwarfs. This is distinct from the aforementioned results on dynamical total masses, as the only individual masses in this spectral type range are for two substellar companions to stars measured from absolute astrometry (Gl 802B; Ireland et al. 2008), or relative astrometry combined with radial velocities (HR 7672B; Crepp et al. 2012). There are also a number of stellar model-dependent mass determinations for brown dwarfs in eclipsing systems (Deleuil et al. 2008; Anderson et al. 2011; Bouchy et al. 2011a,b; Johnson et al. 2011; Siverd et al. 2012; Díaz et al. 2013; Montet et al. 2014). However, all of these companions lack the spectral information available for field L and T dwarfs that enables the strongest tests of substellar models.

## 2. Discovery and Astrometric Monitoring of SDSS J1052+4422AB

### 2.1. Keck/NIRC2 LGS AO

We observed SDSS J1052+4422 on 2005 May 1 UT with the then recently commissioned laser guide star adaptive optics (LGS AO) system at the Keck II telescope (Bouchez et al. 2004; Wizinowich et al. 2006; van Dam et al. 2006). We used the facility near-infrared camera NIRC2, obtaining five dithered images in  $K'$  band. SDSS J1052+4422 appeared to be marginally resolved (peanut shaped) in these images, indicating that it was likely a binary. In follow-up imaging on 2006 May 5 UT, SDSS J1052+4422 was more obviously resolved because it had moved to a wider projected separation of 70 mas, as compared to 42 mas in 2005. We obtained data in the Mauna Kea Observatories (MKO)  $J$ ,  $H$ , and  $K_S$  photometric bandpasses (Simons & Tokunaga 2002; Tokunaga et al. 2002) and discovered that while the western component was brighter in  $K_S$  and perhaps  $H$  band, the eastern component was in fact brighter in  $J$  band. In keeping with the convention with previous  $J$ -band flux reversal binaries (e.g., Liu et al. 2006; Looper et al. 2008), we will refer to the component brighter in  $K_S$ -band as the primary (SDSS J1052+4422A).

We continued Keck AO monitoring of SDSS J1052+4422AB in order to determine its orbital parameters and thereby a total dynamical mass. Our observations are a combination of normal imaging and data taken with the 9-hole non-redundant aperture mask installed in the filter wheel of NIRC2 (Tuthill et al. 2006). On some nights we obtained data using the natural guide star (NGS) AO system, because the tip-tilt star is bright enough ( $R \approx 14.6$  mag) and close enough to the target (19'' away) that it can sometimes be used as an NGS. The analysis of our data was the

same regardless of whether we observed in NGS or LGS mode.

Our procedure for reducing and analyzing NIRC2 imaging data is described in detail in our previous work (Dupuy et al. 2009a,b,c, 2010). To summarize briefly, we measure binary parameters using a three-component Gaussian representation of the point-spread function. We derive uncertainties by applying our fitting method to artificial binary images constructed from images of single stars with similar full-width half-maxima (FWHM) and Strehl ratios, as well as by checking the scatter between individual dithered images. We use the NIRC2 astrometric calibration from Yelda et al. (2010), which includes a correction for the nonlinear distortion of the camera and has a pixel scale of  $9.952 \pm 0.002$  mas pixel $^{-1}$  and an orientation for the detector’s  $+y$ -axis of  $+0^\circ 252 \pm 0^\circ 009$  east of north. Analysis of our masking data was performed using a pipeline similar to that used in previous papers containing NIRC2 masking data (e.g., Ireland et al. 2008; Ireland & Kraus 2008) and is described in detail in Section 2.2 of Dupuy et al. (2009c).

A summary of our Keck AO observations is given in Table 1, including the binary separation, position angle (PA), and flux ratio as well as the FWHM and Strehl ratio of our AO images at each epoch. Contour plots of our imaging data are shown in Figure 1, and images of our masking interferograms are shown in Figure 2. At the two epochs where we have data in more than one bandpass our derived binary parameters are consistent within the errors. However, unlike previous binaries we have monitored (e.g., Gl 417BC; Dupuy et al. 2014), our flux ratios for SDSS J1052+4422AB are not always consistent between epochs. The small variations we observe at  $J$  and  $H$  bands are consistent with variability at the  $\approx 0.10$  mag level as implied by the integrated-light variability of 0.06 mag reported by Girardin et al. (2013). In the following analysis we use the weighted average flux ratio for each bandpass, assuming an additional 0.10 mag error added in quadrature to account for variability. This gives  $\Delta J = -0.45 \pm 0.09$  mag,  $\Delta H = 0.06 \pm 0.07$  mag, and  $\Delta K = 0.52 \pm 0.05$  mag. The only other ultracool binary known to have such a large  $J$ -band flux reversal is 2MASS J14044948–3159330AB ( $\Delta J = -0.54 \pm 0.08$  mag; Looper et al. 2008; Dupuy & Liu 2012).

## 2.2. CFHT/WIRCam Astrometry

We have been monitoring SDSS J1052+4422AB as part of the Hawaii Infrared Parallax Program at the CFHT in order to measure the precise distance needed for a dynamical mass determination. Our methods for obtaining high-precision astrometry from the facility near-infrared wide-field imager WIRCam (Puget et al. 2004) are described in detail in Dupuy & Liu (2012). We have obtained a total of 427  $J$ -band images centered on SDSS J1052+4422AB over 21 epochs spanning 6.79 yr. At each epoch, we measured the position of SDSS J1052+4422AB in integrated light along with 30 other stars in the field having signal-to-noise ratios (S/N)  $> 23$ . The subset of 26 stars that appear in the SDSS-DR9 catalog (Ahn et al. 2012) were used for the absolute astrometric calibration of the linear terms (pixel scales in  $x$  and  $y$ , rotation, and shear). We simultaneously fit for the proper motion and parallax of all stars in the field and found no other sources co-moving with

SDSS J1052+4422AB down to  $J = 18.2$  mag. The median and rms of the seeing was  $0''.59 \pm 0''.09$  over our observations, and the S/N of SDSS J1052+4422AB ranged from 80–160. The absolute positions of SDSS J1052+4422AB measured from our CFHT data are listed in Table 2.

Given the 6.8 yr time baseline of our CFHT observations, and the 8.6 yr orbital period of SDSS J1052+4422AB that we determine from our Keck astrometry (Section 3.1), significant orbital motion might be expected to be observed in our integrated-light astrometry. Indeed, we saw an orbital arc in our CFHT residuals that caused a very poor  $\chi^2 = 428.8$  (37 degrees of freedom) in our initial parallax and proper motion fit to the data. Thus, we must combine our resolved orbital analysis from Keck with our CFHT astrometry in order to accurately retrieve the parallax of SDSS J1052+4422AB.

### 3. Measured Properties of SDSS J1052+4422AB

#### 3.1. Orbital Parameters & Parallax

We performed a joint analysis of our two astrometric data sets for SDSS J1052+4422AB: resolved measurements from Keck AO and integrated-light positions from CFHT/WIRCam. All but one of the seven visual binary orbit parameters are shared in common between the Keck and CFHT data. Since our Keck data only gives us the position of one binary component relative to the other, we fit for the total semimajor axis ( $a = a_1 + a_2$ ) that is the sum of the individual component’s semimajor axes about the center of mass. In our CFHT data, we only see the motion of the photocenter, the amplitude of which depends on the flux ratio and mass ratio of the binary. We therefore fit for a photocenter semimajor axis ( $\alpha$ ) that we will later use to derive the system mass ratio. We also fit for the five usual parameters needed for our CFHT parallax data: R.A. zero point and proper motion, Dec. zero point and proper motion, and parallax. Therefore, there are a total of 13 parameters in the joint fit of our Keck and CFHT data.

To determine probability distributions for the orbit and parallax parameters, we performed a Markov Chain Monte Carlo (MCMC) analysis. Unlike our previous work, we used the Python implementation of the affine-invariant ensemble sampler `emcee` v2.1.0 (Foreman-Mackey et al. 2013). This allows for more efficient exploration of our 13-dimensional parameter space than our own custom MCMC tools that used a Metropolis-Hastings jump acceptance criterion with Gibbs sampling. We adopted uniform priors in the logarithms of period and semimajor axis ( $\log P$ ,  $\log a$ ), eccentricity ( $e$ ), argument of periastron ( $\omega$ ), PA of the ascending node ( $\Omega$ ), mean longitude at a reference time ( $\lambda_{\text{ref}}$ ), and the ratio of the photocenter semimajor axis to the total semimajor axis ( $\alpha/a$ ). The reference time is  $t_{\text{ref}} = 2455197.5$  JD (2010 Jan 1 00:00 UT), which is related to the time of periastron passage  $T_0 = t_{\text{ref}} - P \times (\lambda_{\text{ref}} - \omega)/360^\circ$ . We assume randomly distributed viewing angles by adopting an inclination prior uniform in  $\cos i$ . We adopt uniform priors in the proper motion and R.A. and Dec. zero points and a uniform spatial volume prior in the parallax. The latter is justifiable as SDSS J1052+4422 was discovered well above the magnitude limits of the



SDSS survey ( $m_{\text{lim}} - M \approx 3.5 \text{ mag}$ ). The effect of this discovery bias on the parallax prior was considered by Dupuy & Kraus (2013, see their Figure S3), and we find that SDSS J1052+4422 would be well within the uniform space density regime. Regardless, we note that because of the high precision of our measured parallax this choice of prior has an indistinguishable effect on the credible interval of this parameter ( $\leq 0.1\%$ ). In other words, the observational constraints dominate over the prior in determining the posterior distribution of the parallax. We used  $10^3$  walkers of  $10^4$  steps each, saving only every hundredth step and discarding the first 10% of steps as the burn-in time for each walker.

The best-fit parameters and credible intervals derived from our MCMC posterior distributions are given in Table 3. We found an orbital period of  $8.608 \pm 0.025 \text{ yr}$  (0.29% error) and total semimajor axis of  $70.67 \pm 0.24 \text{ mas}$  (0.34% error), and accounting for the slight covariance between these parameters results in an uncertainty in the dynamical total mass of 1.1% from our orbit determination alone. As a check on our new MCMC methods, we performed a separate MCMC analysis on just the Keck data using our own Metropolis-Hastings code (Dupuy et al. 2014). The resulting  $1\sigma$  credible intervals for the seven visual binary parameters were consistent to within a fraction of  $1\sigma$ . The resolved orbit of SDSS J1052+4422AB is shown in Figure 3 along with our Keck astrometry.

The additional parameters we fitted to our integrated-light CFHT data provide the proper motion and parallax relative to our grid of astrometric reference stars, as well as the size of the photocenter’s orbit<sup>2</sup> ( $\alpha = -11.6 \pm 0.6 \text{ mas}$ ). This best-fit solution is shown in Figure 4. In order to compute the distance, we derived a correction to account for the mean parallax of our reference grid from the Besançon model of the Galaxy (Robin et al. 2003). We found  $\pi_{\text{abs}} - \pi_{\text{rel}} = 1.7 \pm 0.3 \text{ mas}$ , where the uncertainty corresponds to the statistical variance in sampling 30 stars in the  $J$ -band magnitude range of our images, according to the much larger modeled Besançon population. Adding this to the relative parallax results in an absolute parallax of  $38.4 \pm 0.7 \text{ mas}$ , corresponding to a distance of  $26.1 \pm 0.5 \text{ pc}$ . Similarly, we computed additive corrections to our proper motions of  $\Delta\mu_{\text{R.A.}} = -6 \pm 3 \text{ mas yr}^{-1}$  and  $\Delta\mu_{\text{Dec.}} = -7 \pm 3 \text{ mas yr}^{-1}$ . As a check, we input our absolute proper motion and parallax to the BANYAN II v1.3 web tool (Malo et al. 2013; Gagné et al. 2014) but found no linkage to the seven kinematic associations in their solar neighborhood model.

---

<sup>2</sup>We quote the photocenter semimajor axis as a negative value because the photocenter motion is the opposite of what is seen in typical pairings of stars, brown dwarfs, or planets. Normally, the less massive component is fainter and thus the center-of-light follows the brighter, more massive component’s motion. In the case of SDSS J1052+4422AB, the center of  $J$ -band light follows the secondary component. This can be seen when comparing Figures 3 and 4 where, e.g., in 2007 the secondary is seen in Keck data to be southeast of the primary and in CFHT data the photocenter shift is also to the southeast.

### 3.2. Dynamical Masses

Combining our measured parallactic distance with the total semimajor axis and orbital period gives a precise total system mass for SDSS J1052+4422AB of  $88 \pm 5 M_{\text{Jup}}$  (6% error). We can also compute the mass ratio and thereby individual component masses by considering the photocenter motion seen in our integrated-light CFHT data. We found the ratio of the photocenter semimajor axis to the total semimajor axis was  $\alpha/a = -0.164 \pm 0.008$ . This ratio is set by the flux ratio and mass ratio of the binary, such that  $\alpha/a = f - \beta$ . The first parameter is the ratio of the secondary’s mass to the total mass,  $f = M_B/(M_A + M_B)$ , and the second parameter is the ratio of secondary’s flux to the total flux,  $\beta = L_B/(L_A + L_B)$ . Our  $J$ -band flux ratio measured from Keck is  $\Delta J = -0.45 \pm 0.09$  mag, which corresponds to  $\beta = 0.602 \pm 0.020$ . Solving for  $f$  gives  $0.438 \pm 0.022$  and thus a mass ratio of  $q \equiv M_B/M_A = 0.78 \pm 0.07$ . This in turn gives individual masses of  $49 \pm 3 M_{\text{Jup}}$  for SDSS J1052+4422A and  $39 \pm 3 M_{\text{Jup}}$  for SDSS J1052+4422B. Therefore, we validate for the first time that assumed primary component in a  $J$ -band flip system is indeed more massive, and the mass ratio is surprisingly low. We also directly determine that both components are unambiguously substellar ( $< 75 M_{\text{Jup}}$ ; Chabrier & Baraffe 1997).

### 3.3. Spectral Types

In order to fully characterize the SDSS J1052+4422AB system and aid in computing bolometric corrections for the components, we have determined the component spectral types through decomposition of its integrated-light spectrum. Burgasser et al. (2008) published a SpeX prism spectrum of SDSS J1052+4422 in integrated light ( $R = 120$ ) which we obtained from the SpeX Prism Libraries.<sup>3</sup> We performed spectral decomposition analysis using the method described in Section 5.2 of Dupuy & Liu (2012). Briefly, we started with all possible pairs of the 178 IRTF/SpeX prism spectra from the library of Burgasser et al. (2010). For each template pairing we determined the scale factors needed to minimize the  $\chi^2$  compared to our observed spectrum. This resulted in a set of  $J$ -,  $H$ -, and  $K$ -band flux ratios for each pairing, which we compared to the flux ratios we measured from our Keck AO images ( $\Delta J = -0.45 \pm 0.09$  mag,  $\Delta H = 0.06 \pm 0.07$  mag, and  $\Delta K = 0.52 \pm 0.05$  mag). We excluded template pairs that disagreed significantly with our measured flux ratios,  $p(\chi^2_{\text{phot}}) < 0.05$ , and then examined the ensemble of template pairs that provided the best spectral matches.

The best match to our spectrum was provided by the templates SDSSp J010752.33+004156.1 (L6) and SDSS J175024.01+422237.8 (T1.5), where we use the infrared types reported by Burgasser et al. (2010). This best-fit spectral template match is shown in Figure 5. The next best matches use primary templates with types ranging from L4.5:: (2MASSW J0820299+450031, typed in the optical as L5 by Kirkpatrick et al. 2000) to L8.5 and secondary templates with types ranging from

---

<sup>3</sup><http://pono.ucsd.edu/~adam/browndwarfs/spexprism>



T0: (SDSS J015141.69+124429.6, typed in the infrared as T1 by Burgasser et al. 2006) to T2.5. We therefore adopt types of  $L6.5 \pm 1.5$  for SDSS J1052+4422A and  $T1.5 \pm 1.0$  for SDSS J1052+4422B.

### 3.4. Bolometric Luminosities

By combining our Keck flux ratios with published MKO system photometry for SDSS J1052+4422AB (Chiu et al. 2006) and our CFHT parallax, we are able to estimate the component luminosities. Given the fact that the flux ratio flips between  $J$  and  $K$  bands, we first consider the bolometric luminosity ( $L_{\text{bol}}$ ) implied by each bandpass separately. We used the polynomial relations between spectral type and bolometric correction (BC) from Liu et al. (2010). To determine the uncertainty in the bolometric correction we allow for spectral type uncertainties in a Monte Carlo fashion, compute the rms, and then add the published rms scatter about the polynomial relation in quadrature. In  $J$  band we find bolometric corrections of  $1.50 \pm 0.16$  mag and  $1.94 \pm 0.24$  mag for the primary and secondary, respectively. This BC difference exactly compensates for the fact that the secondary is brighter in  $J$  band, resulting in nearly identical luminosities of  $\log(L_{\text{bol}}/L_{\odot}) = -4.62 \pm 0.07$  dex and  $-4.62 \pm 0.10$  dex, respectively. Similarly, in  $H$  band where our photometry is consistent with the two components having equal flux, the BC compensates and gives  $\log(L_{\text{bol}}/L_{\odot}) = -4.59 \pm 0.04$  dex and  $-4.64 \pm 0.04$  dex. We find comparable results using  $K$  band of  $\log(L_{\text{bol}}/L_{\odot}) = -4.57 \pm 0.05$  dex and  $-4.63 \pm 0.06$  dex.

We chose to use the luminosities derived from our  $K$  band photometry because it is the least likely to be affected by the variability observed by Girardin et al. (2013) in  $J$  band, and we have many more  $K$ -band flux ratio measurements than at  $J$  or  $H$  bands. Our  $K$ -band flux ratio has the smallest uncertainty, and the scatter in the  $BC_K$  relation (0.08 mag) is almost as small as for  $BC_H$  (0.07 mag). We note however that the  $L_{\text{bol}}$  estimates in all bands are consistent within the uncertainties.

Table 4 provides a summary of all of the directly measured properties of the SDSS J1052+4422AB system. Figure 6 shows the components of SDSS J1052+4422AB on a color–magnitude diagram in comparison to other field L and T dwarfs with measured distances.

## 4. Model-Derived Properties for SDSS J1052+4422AB

With a precisely determined total dynamical mass (6%), component masses (7%), and component luminosities (15%–20%), we can derive all other physical properties ( $T_{\text{eff}}$ ,  $\log g$ , age, etc.) by invoking evolutionary models. Only one set of models currently incorporates cloud dispersal at the L/T transition, which is particularly relevant for SDSS J1052+4422AB. SM08 “hybrid” models assume the photosphere smoothly transitions from cloudy to cloudless as objects cool from effective temperatures of 1400 K to 1200 K. Because SDSS J1052+4422A is expected to be cloudy based on its late-L spectral type, and SDSS J1052+4422B likely still possesses some cloud opacity at the

photosphere, we also consider the SM08 fully cloudy ( $f_{\text{sed}} = 2$ ) and Lyon Dusty (Chabrier et al. 2000) models.

To derive model properties from the individual masses and luminosities only requires a straightforward bilinear interpolation of model tracks. But this could result in very different ages if models do not accurately predict the mass–luminosity relation for our objects. Because we are also interested in deriving properties under the assumption of coevality, we also use our (more precise) total mass and individual luminosities, ignoring our measured mass ratio, to derive properties from evolutionary models in the same fashion as in our previous work (Liu et al. 2008; Dupuy et al. 2009b). In this coeval analysis, at each point on a  $\log(\text{age})$  grid we use the luminosity of each component to calculate their model-predicted mass,  $T_{\text{eff}}$ , surface gravity, radius, lithium abundance, and near-infrared colors. This is done in a Monte Carlo fashion such that we use  $10^3$  values for a component’s  $L_{\text{bol}}$ , resulting in  $10^3$  mass estimates at each age. We then step through each of these  $10^3$   $L_{\text{bol}}$  pairs, considering the full range of ages for that pair, sum the component masses as a function of age, and determine the age that matches the measured total mass by interpolating the curve. This is also done in a Monte Carlo fashion by repeating this step  $10^3$  times using randomly drawn values for the measured  $M_{\text{tot}}$  from our MCMC posterior. This results in  $10^6$  model-derived values for every parameter and accounts for the errors in both  $L_{\text{bol}}$  and  $M_{\text{tot}}$  while appropriately tracking their covariances via the common uncertainty in the distance.

We report the median,  $1\sigma$ , and  $2\sigma$  credible intervals of the model-derived parameter distributions in the case where we used the individual masses and in the case where we used the total mass assuming coevality (Table 5).

#### 4.1. System Age

One of the fundamental predictions of substellar evolutionary models is how luminosity changes with age for a given mass (or changes with mass at a given age). Thus, by measuring the component masses and luminosities of SDSS J1052+4422AB we can test whether models successfully give the same age for the two components. (By a typical field age of  $\sim 1\text{--}10$  Gyr, even large differences in formation time of a few Myr would result in binaries that are coeval to  $\sim 0.001$  dex.) We can also assume that the age is the same and use the individual luminosities and total mass, ignoring our mass ratio, to derive a single best matching model-derived age.

First, we test the widely used, fully cloudy models for coevality. Given our individually measured masses and luminosities, Lyon Dusty models give ages of  $1.01^{+0.15}_{-0.17}$  Gyr and  $0.66^{+0.10}_{-0.12}$  Gyr for the primary and secondary of SDSS J1052+4422AB, respectively. Accounting for the covariance in distance and mass ratio, the age difference is  $\Delta \log t = 0.19 \pm 0.10$  dex,  $2.0\sigma$  discrepant with being coeval. The SM08 cloudy models give similar ages to Lyon Dusty but somewhat more coeval with  $\Delta \log t = 0.16 \pm 0.10$  dex ( $1.6\sigma$  different from coeval). In contrast to both of these cases, the SM08 hybrid models give ages consistent with coevality at  $0.9\sigma$ ,  $\Delta \log t = 0.09 \pm 0.12$  dex.

The more realistic assumption of SM08 hybrid models that clouds disappear as temperatures cool from 1400 K to 1200 K results in higher luminosities at a given mass and age during the transition. This higher luminosity is not simply due to less cloud opacity. The difference in entropy between a cloudy 1400 K brown dwarf and a cloudless 1200 K brown dwarf is greater than the entropy difference of two brown dwarfs at those temperatures that are both cloudy (Saumon & Marley 2008). Therefore, luminosity evolution should appear to slow down as brown dwarfs cool through the L/T transition because it takes longer to shed this excess entropy, causing a phase of increased luminosity compared to either cloudy or cloudless models. This means that the mass–luminosity relation at a given age becomes shallower in the L/T transition, so that a given luminosity ratio could correspond to a mass ratio further from unity, like the one we measured directly ( $0.78 \pm 0.07$ , Section 3.2). Therefore, it is not surprising that the SM08 hybrid models give ages in better agreement with coevality for SDSS J1052+4422AB.

If we force coevality by ignoring our measured mass ratio, then we find single best matching model-derived ages of  $1.11^{+0.17}_{-0.20}$  Gyr (SM08 hybrid) and  $0.84^{+0.10}_{-0.15}$  Gyr (Lyon Dusty). Figure 7 shows the mass–luminosity relation predicted by models at these respective coeval ages, illustrating the fundamental difference in the predicted luminosity evolution between these two models. Over the mass range 40–50  $M_{\text{Jup}}$ , the Lyon Dusty isochrone has a power-law slope of  $\Delta \log L_{\text{bol}} / \Delta \log M = 3.1$ . In contrast, for the SM08 hybrid models this slope is only 1.3. Our directly measured masses for SDSS J1052+4422AB imply a power-law slope  $\Delta \log L_{\text{bol}} / \Delta \log M = 0.6^{+0.6}_{-0.8}$  over the same  $\approx 40\text{--}50 M_{\text{Jup}}$  mass range. Thus, we find a mass–luminosity relation in the L/T transition that is in much better agreement with SM08 hybrid models than fully cloudy models. In fact, our slope seems to be even shallower than the hybrid models and is even nominally consistent with a inverted relation ( $\Delta \log L_{\text{bol}} / \Delta \log M < 0$ ) within the  $1\sigma$  uncertainty.

Finally, we note that another way of framing the coevality test is to compare the model-derived mass ratios with our observed value of  $0.78 \pm 0.07$ . When using just our total dynamical mass and individual luminosities, both cloudy models give similar mass ratios of  $0.94^{+0.05}_{-0.06}$  (SM08) and  $0.94 \pm 0.05$  (Lyon). These are much closer to unity than we observe because the steeper mass–luminosity relation predicted by cloudy models gives a very small difference in mass for a correspondingly small difference in observed luminosity ( $\Delta \log L_{\text{bol}} = 0.07 \pm 0.07$  dex). In comparison, SM08 hybrid models predict a mass ratio of  $0.87^{+0.11}_{-0.09}$  that is somewhat larger than but consistent with our measured value at  $0.9\sigma$ .

## 4.2. Effective Temperature & Surface Gravity

Combining evolutionary model radii with a measured luminosity and mass readily produces estimates of effective temperature ( $T_{\text{eff}} \propto L_{\text{bol}}^{-1/4} R^{-1/2}$ ) and surface gravity ( $g \propto MR^{-2}$ ), respectively. There are only small differences between the radii predicted at a given age by the models considered here ( $\lesssim 3\%$ ), resulting in differences of  $\lesssim 1\%$  in  $T_{\text{eff}}$  and  $\lesssim 0.03$  dex in  $\log g$ . More important to the model-derived radii is whether we force coevality, in which case the secondary

is predicted to be only slightly larger ( $\leq 0.5\%$ ) than the primary. When the two components are allowed to have different ages but correct masses, the model-derived age of the secondary is 0.1–0.3 dex younger ( $1\sigma$  range), so its predicted radius is 3%–6% larger. Therefore, we adopt the coeval model-derived temperatures and surface gravities of SDSS J1052+4422AB, using the SM08 hybrid models that are most consistent with coevality.

The model-derived temperature of the  $L6.5 \pm 1.5$  spectral type primary is  $1330 \pm 30$  K, while the  $T1.5 \pm 1.0$  secondary is  $1270^{+40}_{-30}$  K. Their predicted surface gravities are  $\log g = 5.10^{+0.05}_{-0.04}$  dex and  $5.04^{+0.05}_{-0.04}$  dex, respectively. Interestingly, the mean evolutionary model-derived temperature of the two components ( $\approx 1300$  K in both coeval and non-coeval cases) is in excellent agreement with the atmospheric model fitting results of the integrated-light 1–14.5  $\mu\text{m}$  spectrum of SDSS J1052+4422AB from Stephens et al. (2009) who found  $T_{\text{eff}} = 1300$  K (acceptable range of 1200–1400 K) and  $\log g = 5.5$  dex (5.0–5.5 dex). A similar agreement between evolutionary and atmospheric model temperatures has been seen for the only other L/T transition brown dwarf with a dynamical mass determination (LHS 2397aB,  $T_{\text{eff}}^{\text{evol}} = 1430 \pm 40$  K and  $T_{\text{eff}}^{\text{atm}} = 1400$  K; Dupuy et al. 2009c). Finally, we note that the model-derived temperatures for SDSS J1052+4422AB align very well with the assumption made in SM08 hybrid models that the L/T transition occurs over the temperature range 1200–1400 K.

### 4.3. Near-infrared Colors

We have independently measured the  $JHK$  colors of the components of SDSS J1052+4422AB by combining our Keck flux ratios with the photometry from Chiu et al. (2006). All colors agree within  $1\sigma$  of the predictions of the SM08 hybrid models whether we enforce coevality or not, although there is somewhat better agreement when deriving colors directly from the individual masses and luminosities (non-coeval). This agreement is remarkable as all other ultracool dwarfs with dynamical mass determinations to date have typically shown  $\gtrsim 0.3$  mag disagreements with models (e.g., Liu et al. 2008; Dupuy et al. 2009b, 2010, 2014). For example, the Lyon Dusty models predict  $\approx 3$ –4 mag redder  $J - K$  colors for the components of SDSS J1052+4422AB, which is not surprising given their assumption of maximal dust clouds. The reason that the SM08 hybrid models agree with our observed  $JHK$  colors is because these evolutionary models also predict a  $J$ -band flux reversal for a system like SDSS J1052+4422AB. The model-derived flux ratios from the individual masses and luminosities are  $\Delta J = -0.50^{+0.15}_{-0.17}$  mag and  $\Delta K = 0.27^{+0.23}_{-0.25}$  mag, which are quite similar to our measured values ( $\Delta J = -0.45 \pm 0.09$  mag,  $\Delta K = 0.52 \pm 0.05$  mag). Figure 8 shows our observed colors and magnitudes for SDSS J1052+4422AB compared to SM08 hybrid evolutionary model tracks.

#### 4.4. Lithium Depletion

According to Chabrier et al. (1996), most of the initial supply of a  $\geq 0.06 M_{\odot}$  brown dwarf’s lithium is destroyed via fusion by an age of  $\leq 0.26$  Gyr, and 99% is destroyed by  $\leq 1.00$  Gyr. The component masses of SDSS J1052+4422AB are  $0.047 \pm 0.003 M_{\odot}$  and  $0.037^{+0.002}_{-0.003}$ , so the Lyon models predict that they should have retained almost all of their lithium ( $\text{Li}/\text{Li}_0 \geq 0.55$  at  $2\sigma$  for the primary). However, even if both components of SDSS J1052+4422AB are lithium bearing, they may not possess a significant amount of atomic lithium that would be readily detectable via the Li I doublet at 6708 Å. At temperatures  $\lesssim 1500$  K, most lithium in the photosphere ( $\approx 1$  bar) is predicted to be locked up in molecular LiCl (Lodders 1999). Thus, given the  $2\sigma$  upper limit on our model-derived temperature for SDSS J1052+4422A ( $T_{\text{eff}} < 1390$  K) it is theoretically expected that both components of SDSS J1052+4422AB are chemically depleted in their atomic lithium. On the other hand, a homogeneous analysis of L and T dwarf optical spectra by Kirkpatrick et al. (2008) found that the occurrence of lithium absorption is highest at L6–L7 spectral types, overlapping with the  $L6.5 \pm 1.5$  spectral type of SDSS J1052+4422A. Moreover, Faherty et al. (2014) detected lithium absorption in WISE J104915.57–531906.1B (T0.5; Burgasser et al. 2013), which is now the only T dwarf known to possess lithium. Notably, King et al. (2010) do not detect lithium in  $\epsilon$  Indi Ba (T1), although this may be due to the fact that it is massive enough to have depleted its lithium (Cardoso et al. 2009). Thus, it is unclear whether SDSS J1052+4422AB would show evidence for atomic lithium in its integrated-light spectrum. High-resolution optical spectroscopy of SDSS J1052+4422AB would provide a unique, joint test of the theoretical lithium-fusing mass-limit and atmospheric model predictions of the chemical depletion of lithium.

### 5. Conclusions

We have discovered that SDSS J1052+4422AB (L6.5+T1.5) is a *J*-band flux reversal binary. We present precise individual dynamical masses by combining resolved Keck AO orbital monitoring spanning 9.0 yr with integrated-light CFHT/WIRCam astrometric monitoring spanning 6.8 yr, the first such masses for any field L or T dwarfs. Despite spectral types that are similar and luminosities that are indistinguishable within the errors, we find a surprisingly low mass ratio of  $q = 0.78 \pm 0.07$ . The only ultracool dwarf binary with a more precise mass ratio is LHS 1070BC ( $0.92 \pm 0.01$  Köhler et al. 2012), also measured from astrometry, which highlights the greater potential of astrometry for measuring precise individual masses as compared to radial velocities. For example, our mass ratio is based on a total of only 2.4 hr of integration time on a 4-m-class telescope, yet it is more precise than the  $q = 0.71^{+0.19}_{-0.13}$  measured for the  $\approx 5$  mag brighter binary Gl 569Bab from numerous resolved spectroscopic observations from Keck (Zapatero Osorio et al. 2004; Simon et al. 2006; Konopacky et al. 2010). Combining our CFHT mass ratio and Keck AO total mass gives component masses of  $49 \pm 3 M_{\text{Jup}}$  for SDSS J1052+4422A ( $L6.5 \pm 1.5$ ) and  $39 \pm 3 M_{\text{Jup}}$  for SDSS J1052+4422B ( $T1.5 \pm 1.0$ ).

This is the first *J*-band flux reversal binary or high-amplitude variable with a dynamical mass

measurement, providing a precise benchmark for the cloud dispersal phase of substellar evolution. We validate that the component fainter in  $J$  band is in fact more massive and that both components are unambiguously substellar ( $<75 M_{\text{Jup}}$ ). Perhaps the most striking result is the shallow mass–luminosity relation in the L/T transition implied by our data ( $\Delta \log L_{\text{bol}}/\Delta \log M = 0.6^{+0.6}_{-0.8}$  over  $\approx 40\text{--}50 M_{\text{Jup}}$ ). This disagrees with the mass–luminosity relation predicted by fully cloudy models, providing the first direct observational support that cloud dispersal plays an important role in luminosity evolution. We quantify this as a coevality test using our measured individual masses and luminosities to derive an age from evolutionary models for each component and test if the models successfully give the same age for both components. Lyon Dusty models give ages that are different by  $0.19 \pm 0.10$  dex, a  $2.0\sigma$  discrepancy. In comparison, hybrid models from Saumon & Marley (2008), in which the dispersal of clouds causes a slowing of luminosity evolution, gives component ages different by  $0.09 \pm 0.12$  dex and thus consistent at  $(0.9\sigma)$ .

In fact, these SM08 hybrid evolutionary models paint a remarkably self-consistent picture for the properties of SDSS J1052+4422AB. The models assume that clouds disperse as temperatures cool from 1400 K to 1200 K. From our measured luminosities and SM08 model-derived radii we find  $T_{\text{eff}} = 1330 \pm 30$  K for the  $L6.5 \pm 1.5$  primary and  $1270^{+40}_{-30}$  K for the  $T1.5 \pm 1.0$  secondary. SM08 hybrid models also accurately predict the  $JHK$  colors of the components, including the reversal in flux ratio observed between  $J$  and  $K$  bands. In addition, the  $T_{\text{eff}}$  of 1300 K found for SDSS J1052+4422AB by Stephens et al. (2009), who used the same atmospheres in their spectral synthesis modeling as are used by SM08 evolutionary models, is in excellent agreement with our temperatures derived from luminosities and model radii. We note that without an independent measurement of the age of SDSS J1052+4422AB, we cannot rule out a constant systematic offset in the SM08 hybrid model luminosities, as our coevality test only constrains slope of the mass–luminosity relation. For example, mid-L dwarfs appear to be 0.2–0.4 dex more luminous than predicted by models at a given mass and age (Dupuy et al. 2009b, 2014). If this holds true for L/T transition objects, then the age we derive from SM08 models would be underestimated by a factor of  $\approx 2\text{--}3$ .

Overall, it seems that the distinguishing features SDSS J1052+4422AB, like a  $J$ -band flux reversal and high-amplitude variability, are normal for a field L/T binary caught during the process of cloud dispersal. SDSS J1052+4422AB’s model-derived age of  $1.11^{+0.17}_{-0.20}$  Gyr is typical of field brown dwarfs (e.g., Zapatero Osorio et al. 2007), and the component surface gravities are correspondingly unexceptional,  $\log g = 5.0\text{--}5.2$  dex. The one unexpected physical property is the low mass ratio. To determine if this is a typical feature of L/T transition binaries, especially for  $J$ -band flux reversal systems, will require more individual mass measurements for late-L to early-T type brown dwarfs. Fortunately, such masses will likely be available in the near future as our CFHT astrometric monitoring continues. Orbit determinations typically require  $\approx 30\%$  coverage of the orbital period, and we have been obtaining CFHT data on our Keck dynamical mass sample for  $\approx 8$  yr. Thus, L/T binaries with orbital periods  $\lesssim 20$  yr should soon have photocenter semimajor axis measurements that will enable precise individual dynamical masses to further map out the



substellar mass–luminosity relation.

Our results lend further support to the growing evidence that clouds have a significant impact on the luminosity evolution of substellar objects. A shallow mass–luminosity relation in the L/T transition suggests that even when the age and luminosity of an object are constrained its mass may be difficult to estimate precisely. This adds another obstacle to estimating masses for directly imaged extrasolar planets in this spectral type range (e.g., HR 8799b; Bowler et al. 2010; Barman et al. 2011). The L/T transition corresponds to the breakup of mostly silicate and iron clouds. At cooler temperatures, clouds composed of sulfides emerge ( $T_{\text{eff}} \lesssim 900$  K; Morley et al. 2012) and water ice clouds possibly at  $\lesssim 350$  K (Morley et al. 2014). Even though sulfide clouds are expected to be thinner, in principle they could impact luminosity evolution in a comparable way as we have now observed for silicate clouds, implying similar alterations to the mass–luminosity relation for much colder brown dwarfs. Directly measured individual masses for late-T and Y dwarf binaries should be able to test this idea.

We thank the referee for a timely and very helpful review. It is a pleasure to thank Antonin Bouchez, David LeMignant, Marcos van Dam, Randy Campbell, Gary Punawai, Peter Wizinowich, and the Keck Observatory staff for their efforts assisting on our first LGS AO night that resulted in the discovery of SDSS J1052+4422AB. We also thank Joel Aycock, Al Conrad, Greg Doppmann, Heather Hershley, Jim Lyke, Jason McIlroy, Julie Riviera, Hien Tran, and Cynthia Wilburn for assistance with subsequent Keck LGS AO observing. We greatly appreciate the CFHT staff for their constant observing support and dedication to delivering the highest quality data products. This work was supported by a NASA Keck PI Data Award, administered by the NASA Exoplanet Science Institute. M.C.L. acknowledges support from NSF grant AST09-09222. Our research has employed the 2MASS data products; NASA’s Astrophysical Data System; the SIMBAD database operated at CDS, Strasbourg, France; and the SpeX Prism Spectral Libraries, maintained by Adam Burgasser at <http://www.browndwarfs.org/spexprism>. Finally, the authors wish to recognize and acknowledge the very significant cultural role and reverence that the summit of Mauna Kea has always had within the indigenous Hawaiian community. We are most fortunate to have the opportunity to conduct observations from this mountain.

*Facilities:* Keck:II (LGS AO, NGS AO, NIRC2), CFHT (WIRCam) IRTF (SpeX)

## REFERENCES

- Ahn, C. P., Alexandroff, R., Allende Prieto, C., et al. 2012, [ApJS](#), **203**, 21
- Anderson, D. R., Collier Cameron, A., Hellier, C., et al. 2011, [ApJ](#), **726**, L19
- Artigau, É., Bouchard, S., Doyon, R., & Lafrenière, D. 2009, [ApJ](#), **701**, 1534
- Baraffe, I., Chabrier, G., Barman, T. S., Allard, F., & Hauschildt, P. H. 2003, [A&A](#), **402**, 701
- Barman, T. S., Macintosh, B., Konopacky, Q. M., & Marois, C. 2011, [ApJ](#), **733**, 65
- Bouchez, A. H., Le Mignant, D., van Dam, M. A., et al. 2004, in [Society of Photo-Optical Instrumentation Engineers \(SPIE\) Conference Series](#), Vol. 5490, [Advancements in Adaptive Optics](#), ed. D. Bonaccini Calia, B. L. Ellerbroek, & R. Ragazzoni, 321
- Bouchy, F., Bonomo, A. S., Santerne, A., et al. 2011a, [A&A](#), **533**, A83
- Bouchy, F., Deleuil, M., Guillot, T., et al. 2011b, [A&A](#), **525**, A68
- Bouy, H., et al. 2004, [A&A](#), **423**, 341
- Bouy, H., Bertin, E., Sarro, L. M., et al. 2015, ArXiv e-prints, [arXiv:1502.03728 \[astro-ph.SR\]](#)
- Bowler, B. P., Liu, M. C., Dupuy, T. J., & Cushing, M. C. 2010, [ApJ](#), **723**, 850
- Burgasser, A. J., Cruz, K. L., Cushing, M., et al. 2010, [ApJ](#), **710**, 1142
- Burgasser, A. J., Geballe, T. R., Leggett, S. K., Kirkpatrick, J. D., & Golimowski, D. A. 2006, [ApJ](#), **637**, 1067
- Burgasser, A. J., Liu, M. C., Ireland, M. J., Cruz, K. L., & Dupuy, T. J. 2008, [ApJ](#), **681**, 579
- Burgasser, A. J., Sheppard, S. S., & Luhman, K. L. 2013, [ApJ](#), **772**, 129
- Burgasser, A. J., Kirkpatrick, J. D., Brown, M. E., et al. 2002, [ApJ](#), **564**, 421
- Burrows, A., Marley, M., Hubbard, W. B., et al. 1997, [ApJ](#), **491**, 856
- Cardoso, C. V., McCaughrean, M. J., King, R. R., et al. 2009, in [American Institute of Physics Conference Series](#), Vol. 1094, [American Institute of Physics Conference Series](#), ed. E. Stempels, 509
- Chabrier, G., & Baraffe, I. 1997, [A&A](#), **327**, 1039
- Chabrier, G., Baraffe, I., Allard, F., & Hauschildt, P. 2000, [ApJ](#), **542**, 464
- Chabrier, G., Baraffe, I., & Plez, B. 1996, [ApJ](#), **459**, L91
- Chauvin, G., Lagrange, A.-M., Dumas, C., et al. 2004, [A&A](#), **425**, L29

- Chiu, K., Fan, X., Leggett, S. K., et al. 2006, [AJ](#), **131**, 2722
- Crepp, J. R., Johnson, J. A., Fischer, D. A., et al. 2012, [ApJ](#), **751**, 97
- Dahn, C. C., Harris, H. C., Vrba, F. J., et al. 2002, [AJ](#), **124**, 1170
- Deleuil, M., Deeg, H. J., Alonso, R., et al. 2008, [A&A](#), **491**, 889
- Díaz, R. F., Damiani, C., Deleuil, M., et al. 2013, [A&A](#), **551**, L9
- Dupuy, T. J., & Kraus, A. L. 2013, [Science](#), **341**, 1492
- Dupuy, T. J., & Liu, M. C. 2012, [ApJS](#), **201**, 19
- Dupuy, T. J., Liu, M. C., & Bowler, B. P. 2009a, [ApJ](#), **706**, 328
- Dupuy, T. J., Liu, M. C., Bowler, B. P., et al. 2010, [ApJ](#), **721**, 1725
- Dupuy, T. J., Liu, M. C., & Ireland, M. J. 2009b, [ApJ](#), **692**, 729
- . 2009c, [ApJ](#), **699**, 168
- . 2014, [ApJ](#), **790**, 133
- Faherty, J. K., Beletsky, Y., Burgasser, A. J., et al. 2014, [ApJ](#), **790**, 90
- Foreman-Mackey, D., Hogg, D. W., Lang, D., & Goodman, J. 2013, [PASP](#), **125**, 306
- Freytag, B., Allard, F., Ludwig, H.-G., Homeier, D., & Steffen, M. 2010, [A&A](#), **513**, A19
- Gagné, J., Lafrenière, D., Doyon, R., Malo, L., & Artigau, É. 2014, [ApJ](#), **783**, 121
- Geballe, T. R., Knapp, G. R., Leggett, S. K., et al. 2002, [ApJ](#), **564**, 466
- Girardin, F., Artigau, É., & Doyon, R. 2013, [ApJ](#), **767**, 61
- Gizis, J. E., Reid, I. N., Knapp, G. R., et al. 2003, [AJ](#), **125**, 3302
- Helling, C., & Casewell, S. 2014, [A&A Rev.](#), **22**, 80
- Ireland, M. J., Kraus, A., Martinache, F., Lloyd, J. P., & Tuthill, P. G. 2008, [ApJ](#), **678**, 463
- Ireland, M. J., & Kraus, A. L. 2008, [ApJ](#), **678**, L59
- Johnson, J. A., Apps, K., Gazak, J. Z., et al. 2011, [ApJ](#), **730**, 79
- King, R. R., McCaughrean, M. J., Homeier, D., et al. 2010, [A&A](#), **510**, A99
- Kirkpatrick, J. D., Reid, I. N., Liebert, J., et al. 2000, [AJ](#), **120**, 447
- Kirkpatrick, J. D., Cruz, K. L., Barman, T. S., et al. 2008, [ApJ](#), **689**, 1295

- Knapp, G. R., Leggett, S. K., Fan, X., et al. 2004, [AJ](#), **127**, 3553
- Köhler, R., Ratzka, T., & Leinert, C. 2012, [A&A](#), **541**, A29
- Konopacky, Q. M., Ghez, A. M., Barman, T. S., et al. 2010, [ApJ](#), **711**, 1087
- Lane, B. F., Zapatero Osorio, M. R., Britton, M. C., Martín, E. L., & Kulkarni, S. R. 2001, [ApJ](#), **560**, 390
- Leggett, S. K., Golimowski, D. A., Fan, X., et al. 2002, [ApJ](#), **564**, 452
- Liu, M. C., Dupuy, T. J., & Ireland, M. J. 2008, [ApJ](#), **689**, 436
- Liu, M. C., Dupuy, T. J., & Leggett, S. K. 2010, [ApJ](#), **722**, 311
- Liu, M. C., Leggett, S. K., Golimowski, D. A., et al. 2006, [ApJ](#), **647**, 1393
- Liu, M. C., Magnier, E. A., Deacon, N. R., et al. 2013, [ApJ](#), **777**, L20
- Lodders, K. 1999, [ApJ](#), **519**, 793
- Lodieu, N., Boudreault, S., & Béjar, V. J. S. 2014, [MNRAS](#), **445**, 3908
- Looper, D. L., Gelino, C. R., Burgasser, A. J., & Kirkpatrick, J. D. 2008, [ApJ](#), **685**, 1183
- Malo, L., Doyon, R., Lafrenière, D., et al. 2013, [ApJ](#), **762**, 88
- Marley, M. S., & Robinson, T. D. 2014, ArXiv e-prints, [arXiv:1410.6512 \[astro-ph.EP\]](#)
- Marois, C., Macintosh, B., Barman, T., et al. 2008, [Science](#), **322**, 1348
- Marois, C., Zuckerman, B., Konopacky, Q. M., Macintosh, B., & Barman, T. 2010, [Nature](#), **468**, 1080
- Montet, B. T., Johnson, J. A., Muirhead, P. S., et al. 2014, ArXiv e-prints, [arXiv:1411.4047 \[astro-ph.SR\]](#)
- Morley, C. V., Fortney, J. J., Marley, M. S., et al. 2012, [ApJ](#), **756**, 172
- Morley, C. V., Marley, M. S., Fortney, J. J., et al. 2014, [ApJ](#), **787**, 78
- Puget, P., Stadler, E., Doyon, R., et al. 2004, in [Society of Photo-Optical Instrumentation Engineers \(SPIE\) Conference Series](#), ed. A. F. M. Moorwood & M. Iye, Vol. 5492, 978
- Radigan, J., Jayawardhana, R., Lafrenière, D., et al. 2012, [ApJ](#), **750**, 105
- Radigan, J., Lafrenière, D., Jayawardhana, R., & Artigau, E. 2014, [ApJ](#), **793**, 75
- Robin, A. C., Reylé, C., Derrière, S., & Picaud, S. 2003, [A&A](#), **409**, 523

- Saumon, D., & Marley, M. S. 2008, [ApJ](#), 689, 1327
- Seifahrt, A., Röhl, T., Neuhäuser, R., et al. 2008, [A&A](#), 484, 429
- Simon, M., Bender, C., & Prato, L. 2006, [ApJ](#), 644, 1183
- Simons, D. A., & Tokunaga, A. 2002, [PASP](#), 114, 169
- Siverd, R. J., Beatty, T. G., Pepper, J., et al. 2012, [ApJ](#), 761, 123
- Stassun, K. G., Mathieu, R. D., & Valenti, J. A. 2006, [Nature](#), 440, 311
- Stephens, D. C., Leggett, S. K., Cushing, M. C., et al. 2009, [ApJ](#), 702, 154
- Tinney, C. G., Burgasser, A. J., & Kirkpatrick, J. D. 2003, *AJ*, 126, 975
- Tokunaga, A. T., Simons, D. A., & Vacca, W. D. 2002, [PASP](#), 114, 180
- Tsuji, T., & Nakajima, T. 2003, [ApJ](#), 585, L151
- Tuthill, P., Lloyd, J., Ireland, M., et al. 2006, in *Society of Photo-Optical Instrumentation Engineers (SPIE) Conference Series, Vol. 6272, Advances in Adaptive Optics II*, ed. B. L. Ellerbroek & D. Bonaccini Calia, 103
- van Dam, M. A., Bouchez, A. H., Le Mignant, D., et al. 2006, [PASP](#), 118, 310
- Wizinowich, P. L., Le Mignant, D., Bouchez, A. H., et al. 2006, [PASP](#), 118, 297
- Yelda, S., Lu, J. R., Ghez, A. M., et al. 2010, [ApJ](#), 725, 331
- Zapatero Osorio, M. R., Lane, B. F., Pavlenko, Y., et al. 2004, [ApJ](#), 615, 958
- Zapatero Osorio, M. R., Martín, E. L., Béjar, V. J. S., et al. 2007, [ApJ](#), 666, 1205

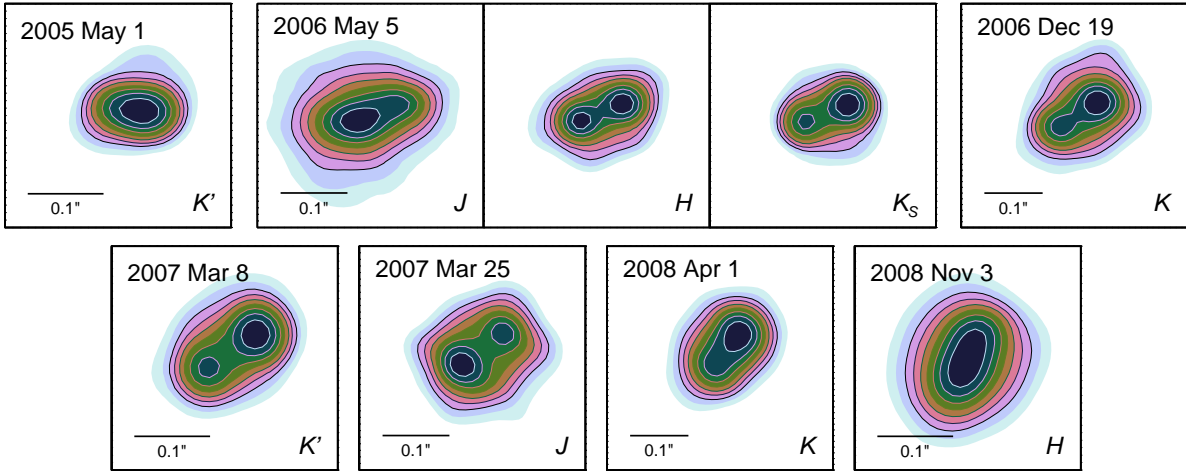


Fig. 1.— Contour plots of our Keck AO images from which we derive astrometry and flux ratios (Table 1). Contours are in logarithmic intervals from unity to 10% of the peak flux in each band. The image cutouts are all the same size and have the same native pixel scale, and we have rotated them such that north is up for display purposes.



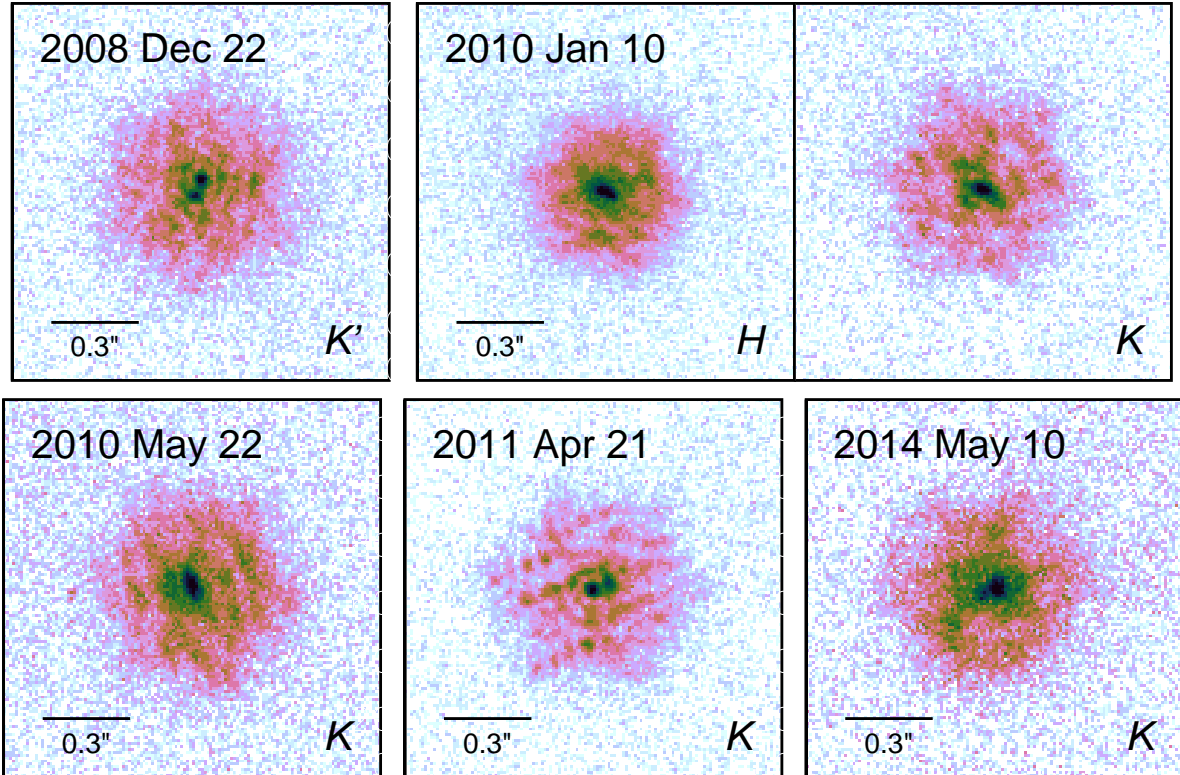


Fig. 2.— Keck/NIRC2 images of the interferograms produced when observing SDSS J1052+4422AB with the 9-hole aperture mask. The binary can be seen by eye as an elongation or double peak in the center of the point-spread function in all but one epoch. In data from 2010 May 22 UT the binary is very tight ( $39.9 \pm 0.7$  mas), and the elongation is instead along the elevation axis ( $205^\circ$ ) caused by atmospheric dispersion given the modest airmass (1.32) of the observation. These image cutouts are all the same size, have the same native pixel scale, have been rotated such that north is up, and are shown with a square-root stretch.

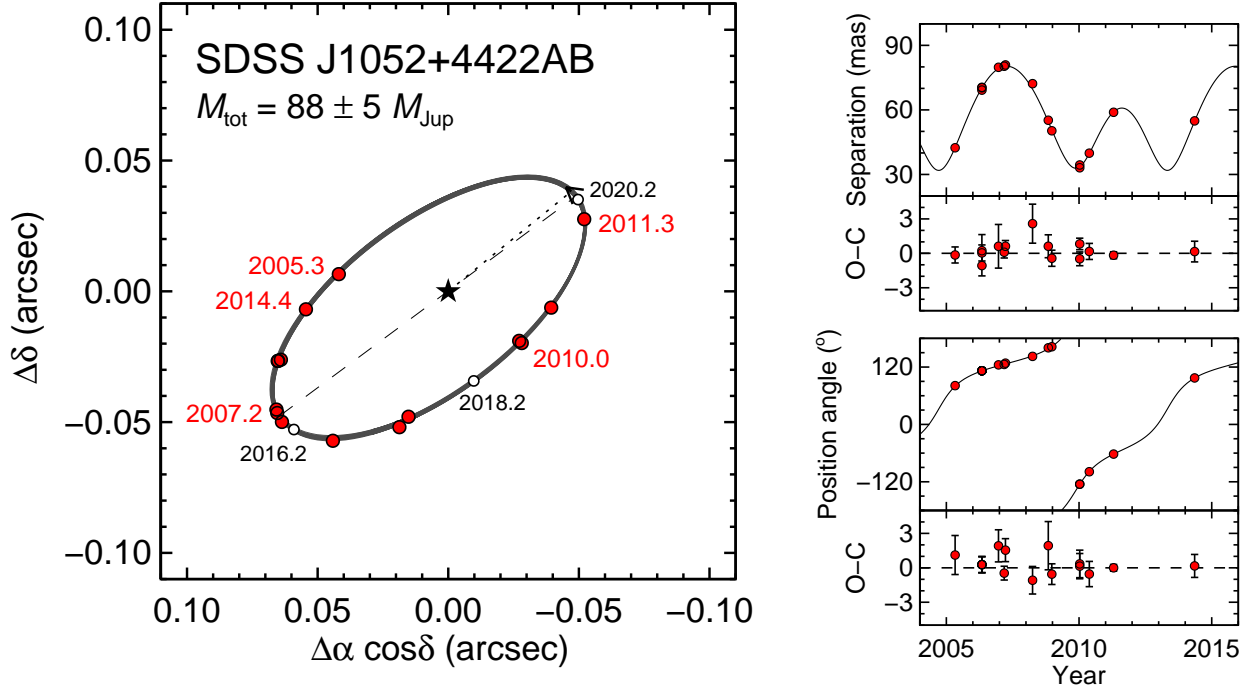


Fig. 3.— *Left:* Keck AO relative astrometry for SDSS J1052+4422AB along with 100 randomly drawn orbits from our MCMC analysis individually plotted as thin lines. Error bars for the data points are smaller than the plotting symbols. The short dotted line indicates the time of periastron passage, the long dashed line shows the line of nodes, and small empty circles show predicted future locations. *Right:* Measurements of the projected separation and PA of SDSS J1052+4422AB. The best-fit orbit is shown as a solid line. The bottom panels show the observed minus computed ( $O - C$ ) measurements with observational error bars.

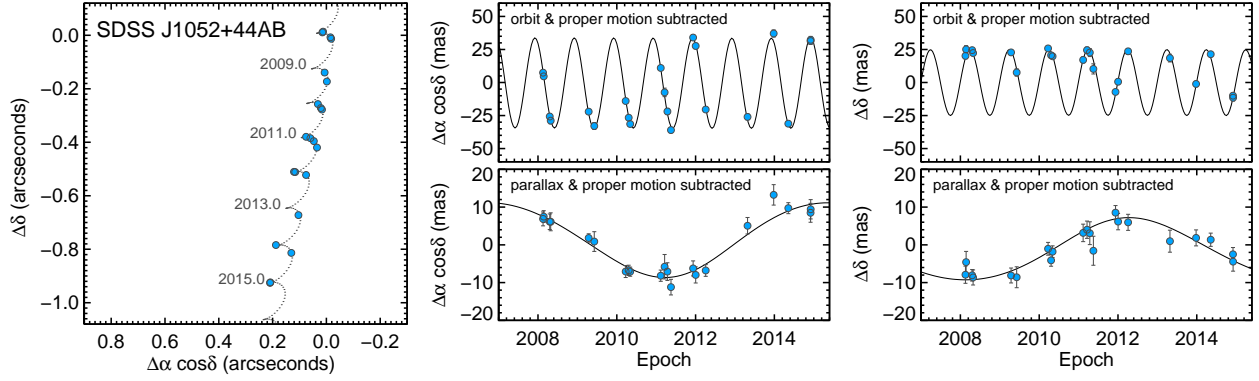


Fig. 4.— *Left*: CFHT/WIRCam integrated-light astrometry for SDSS J1052+4422AB (blue circles) along with the best-fit model incorporating proper motion, parallax, and photocenter orbital motion (dotted line). *Middle, Right*: The same astrometry except with the best-fit proper motion and orbital motion removed, leaving just the parallax (top), and with the best-fit proper motion and parallax removed, leaving just the orbital motion of the photocenter (bottom). Error bars are plotted on all panels, but they are typically only visible in the plots displaying orbital motion.

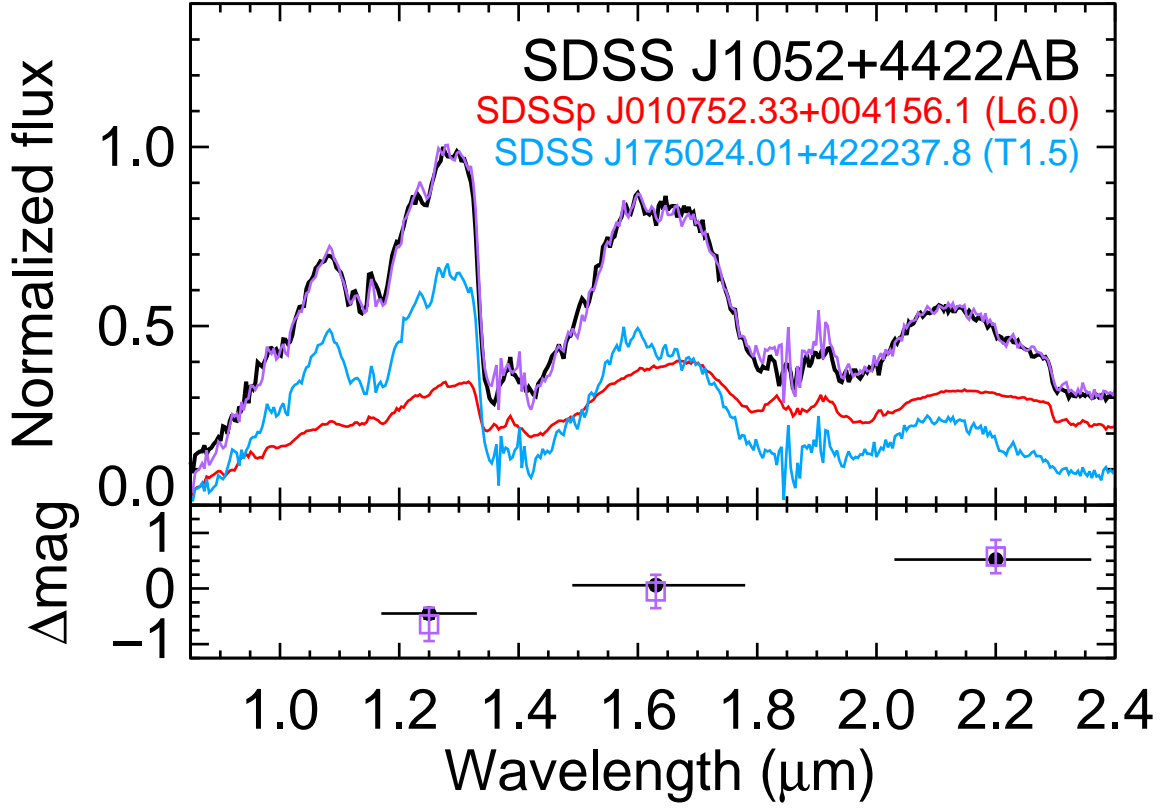


Fig. 5.— Integrated-light spectrum of SDSS J1052+4422AB (black) and best matching component templates (colored lines). The bottom subpanel shows the observed  $J$ -,  $H$ -, and  $K$ -band broadband flux ratios used to constrain the decomposition (filled black circles with errors) and the resulting flux ratios computed from the best matching template pair (open colored squares).

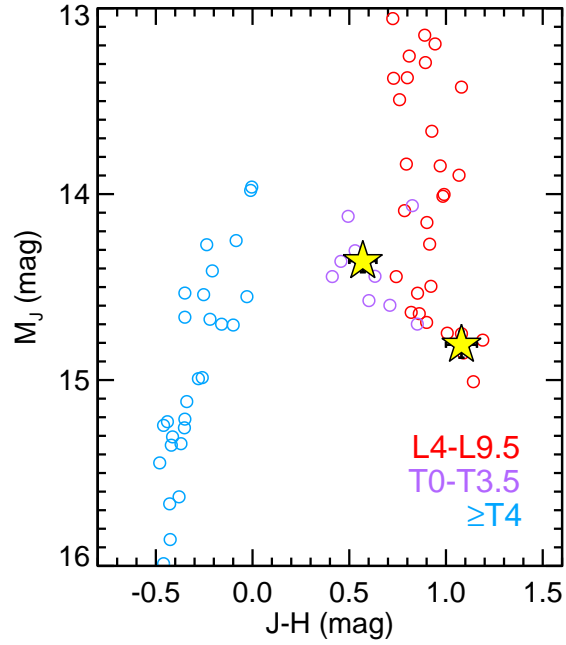


Fig. 6.— Color-magnitude diagram showing the components of SDSS J1052+4422AB (yellow stars) along with field L and T dwarfs with measured distances (open circles). Both components have typical colors and magnitudes for their spectral types ( $L6.5 \pm 1.5$  and  $T1.5 \pm 1.0$ ). Photometry is on the MKO system. Field dwarf data were obtained from the Database of Ultracool Parallaxes (<http://www.as.utexas.edu/~tdupuy/plx/>; Dupuy & Liu 2012), and we only plot objects with uncertainties  $<10\%$  in parallax and  $<0.10$  mag in color.

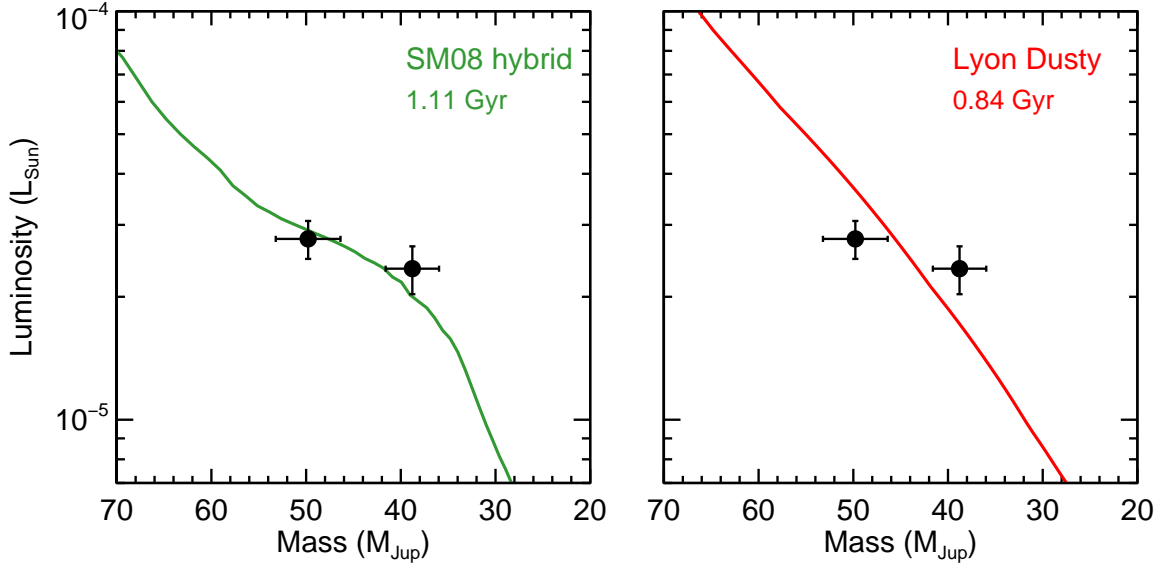


Fig. 7.— Our directly measured individual masses and luminosities for the components of SDSS J1052+4422AB compared to predictions from SM08 hybrid (left) and Lyon Dusty (right) evolutionary models. Model tracks are shown for the single coeval system age that best matches the total mass and individual luminosities. The unexpectedly shallow mass–luminosity relation implied by our data are better described by the SM08 hybrid models that show a slowing of luminosity evolution for objects in the L/T transition, while Lyon Dusty models are inconsistent with coevality at  $2.0\sigma$ . (Note that we do not plot a confidence range for models as that would effectively be double-plotting our errors, since the age of the plotted isochrone is derived from our observed total mass and component luminosities.)



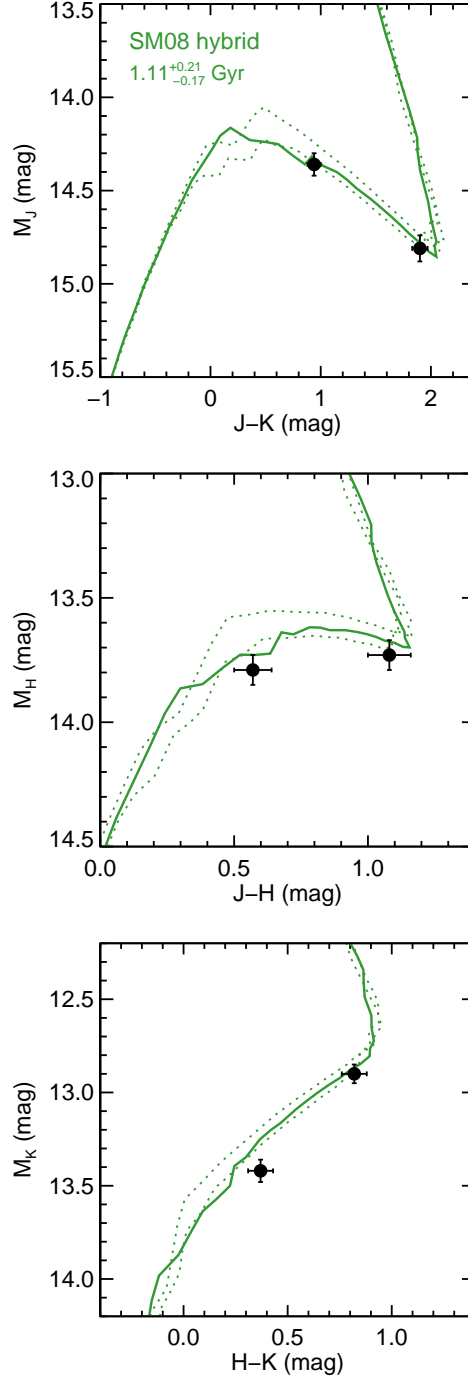


Fig. 8.— Measured colors and absolute magnitudes of the components of SDSS J1052+4422AB compared to predictions from SM08 hybrid evolutionary models. Model tracks are shown for the coeval system age that best matches the total mass and individual luminosities (solid) and ages at  $\pm 1\sigma$  of this value (dotted). Unlike previous generations of evolutionary models, the predicted colors and magnitudes of SM08 hybrid match our observations remarkably well.

Table 1. Relative astrometry and photometry for SDSS J1052+4422AB from Keck/NIRC2 AO

Date (UT)	Airmass	Filter	FWHM (mas)	Strehl ratio	$\rho$ (mas)	PA ( $^{\circ}$ )	$\Delta m$ (mag)
2005 May 1	1.342	$K'$	$53 \pm 2$	$0.27 \pm 0.02$	$42.4 \pm 0.7$	$81.1 \pm 1.7$	$0.51 \pm 0.03$
2006 May 5	1.544	$J$	$57 \pm 7$	$0.045 \pm 0.008$	$69.2 \pm 0.9$	$112.2 \pm 0.7$	$-0.61 \pm 0.11$
2006 May 5	1.572	$H$	$51 \pm 3$	$0.11 \pm 0.02$	$70.5 \pm 1.4$	$112.2 \pm 0.7$	$0.00 \pm 0.13$
2006 May 5	1.274	$K_S$	$54 \pm 2$	$0.32 \pm 0.06$	$70.3 \pm 0.7$	$112.2 \pm 0.7$	$0.49 \pm 0.05$
2006 Dec 19	1.099	$K$	$66 \pm 6$	$0.16 \pm 0.05$	$79.8 \pm 1.9$	$124.5 \pm 1.4$	$0.49 \pm 0.15$
2007 Mar 8	1.102	$K'$	$59 \pm 5$	$0.20 \pm 0.04$	$80.3 \pm 0.5$	$125.4 \pm 0.6$	$0.45 \pm 0.06$
2007 Mar 25	1.102	$J$	$52 \pm 6$	$0.049 \pm 0.016$	$80.9 \pm 0.5$	$128.1 \pm 1.0$	$-0.36 \pm 0.05$
2008 Apr 1	1.582	$K$	$69 \pm 2$	$0.16 \pm 0.05$	$72.2 \pm 1.7$	$142.3 \pm 1.2$	$0.42 \pm 0.07$
2008 Nov 3	1.373	$H$	$57 \pm 4$	$0.08 \pm 0.02$	$55.2 \pm 1.0$	$160.2 \pm 2.1$	$-0.01 \pm 0.07$
2008 Dec 22	1.132	$K'$	...	...	$50.3 \pm 0.7$	$162.4 \pm 0.9$	$0.51 \pm 0.03$
2010 Jan 10	1.188	$H$	...	...	$34.4 \pm 0.5$	$234.9 \pm 1.1$	$0.14 \pm 0.03$
2010 Jan 10	1.169	$K$	...	...	$33.1 \pm 0.6$	$235.1 \pm 1.2$	$0.57 \pm 0.05$
2010 May 22	1.316	$K$	...	...	$39.9 \pm 0.7$	$261.0 \pm 1.1$	$0.56 \pm 0.04$
2011 Apr 21	1.212	$K$	...	...	$58.9 \pm 0.3$	$297.91 \pm 0.29$	$0.545 \pm 0.016$
2014 May 10	1.326	$K$	...	...	$54.9 \pm 0.9$	$97.2 \pm 1.0$	$0.51 \pm 0.04$

Note. — For the Keck imaging data, Strehl ratios and FWHM were computed using the publicly available routine NIRC2STREHL. Masking observations have no FWHM and Strehl listed.

Table 2. Integrated-light astrometry for SDSS J1052+4422AB from CFHT/WIRCam

Date (UT)	R.A. (deg)	Dec. (deg)	$\sigma_{\text{R.A.} \cos \delta}$ (mas)	$\sigma_{\text{Dec.}}$ (mas)	Airmass	Seeing
2008 Feb 17	163.05659646	+44.38217395	1.8	2.3	1.100	0''.55
2008 Feb 23	163.05659550	+44.38217470	1.6	2.8	1.099	0''.59
2008 Apr 19	163.05658483	+44.38216886	2.1	1.5	1.104	0''.60
2008 Apr 28	163.05658379	+44.38216735	2.4	2.0	1.100	0''.53
2009 Apr 15	163.05659324	+44.38213225	1.1	2.0	1.101	0''.59
2009 Jun 6	163.05658999	+44.38212290	2.6	2.8	1.160	0''.62
2010 Mar 24	163.05660297	+44.38209950	1.6	1.7	1.107	0''.90
2010 Apr 21	163.05659864	+44.38209535	1.4	1.6	1.100	0''.62
2010 May 5	163.05659707	+44.38209378	1.2	1.5	1.099	0''.59
2011 Feb 12	163.05662003	+44.38206551	1.5	2.3	1.118	0''.62
2011 Mar 20	163.05661377	+44.38206406	3.2	2.3	1.128	0''.67
2011 Apr 15	163.05660884	+44.38206101	2.3	3.0	1.122	0''.83
2011 May 18	163.05660425	+44.38205434	2.1	3.8	1.125	0''.66
2011 Dec 9	163.05663748	+44.38202911	2.0	1.9	1.099	0''.55
2012 Jan 2	163.05663574	+44.38202885	2.1	2.2	1.107	0''.59
2012 Apr 4	163.05662005	+44.38202585	1.6	2.1	1.114	0''.63
2013 Apr 27	163.05663104	+44.38198416	2.2	2.9	1.112	0''.58
2013 Dec 25	163.05666361	+44.38195306	2.7	2.1	1.107	0''.66
2014 May 10	163.05664133	+44.38194490	1.5	1.8	1.116	0''.54
2014 Dec 2	163.05667169	+44.38191431	2.5	1.8	1.104	0''.57
2014 Dec 3	163.05667208	+44.38191378	2.6	2.5	1.121	0''.55

Table 3. Derived orbital and parallax parameters for SDSS J1052+4422AB

Parameter	Best fit	Median	68.3% c.i.	95.4% c.i.
Visual binary orbital parameters				
Orbital period $P$ (yr)	8.614	8.608	8.583, 8.632	8.560, 8.658
Semimajor axis $a$ (mas)	70.59	70.67	70.43, 70.91	70.20, 71.16
Eccentricity $e$	0.1387	0.1399	0.1376, 0.1422	0.1354, 0.1445
Inclination $i$ ( $^\circ$ )	62.0	62.1	61.7, 62.4	61.4, 62.7
PA of the ascending node $\Omega$ ( $^\circ$ )	126.7	126.8	126.5, 127.2	126.2, 127.5
Argument of periastron $\omega$ ( $^\circ$ )	186.5	187.3	185.6, 188.9	184.0, 190.5
Mean longitude at 2455197.5 JD $\lambda_{\text{ref}}$ ( $^\circ$ )	113.4	113.4	112.9, 113.8	112.5, 114.2
Additional integrated-light astrometric parameters				
R.A. – 163.0566182 (mas)	0.0	–0.3	–1.6, 0.9	–2.8, 2.1
Dec. – +44.3821006 (mas)	0.0	0.1	–0.5, 0.7	–1.1, 1.3
Relative proper motion in R.A. $\mu_{\text{R.A.,rel}}$ (mas yr $^{-1}$ )	24.51	24.56	24.36, 24.77	24.16, 24.97
Relative proper motion in Dec. $\mu_{\text{Dec.,rel}}$ (mas yr $^{-1}$ )	–133.96	–133.91	–134.14, –133.69	–134.37, –133.45
Relative parallax $\pi_{\text{rel}}$ (mas)	36.87	36.67	36.06, 37.29	35.42, 37.90
Photocenter semimajor axis $\alpha$ (mas)	–11.7	–11.6	–12.2, –11.0	–12.8, –10.5

Note. — For each parameter we report the value corresponding to the best fit (i.e., the lowest  $\chi^2$  in the MCMC chain,  $\chi^2_{\text{min}} = 50.7$ , 59 degrees of freedom) along with the median of the posterior distribution and the shortest intervals containing 68.3% and 95.4% of the chain steps (i.e.,  $1\sigma$  and  $2\sigma$  credible intervals). The time of periastron passage corresponding to these  $\lambda_{\text{ref}}$  and  $\omega$  posteriors is  $T_0 = 55842 \pm 13$  MJD (2011 Oct 7 UT). For clarity, the R.A. and Dec. zero points are reported relative to their best-fit values. R.A. and Dec. zero points are reported at equinox J2000.0 and epoch 2010.0. Without resolved radial velocities there is a  $180^\circ$  ambiguity in  $\Omega$ ,  $\omega$ , and  $\lambda_{\text{ref}}$ .

Table 4. Measured Properties of SDSS J1052+4422AB

Property	SDSS J1052+4422A	SDSS J1052+4422B	Ref.
$d$ (pc)	$26.1 \pm 0.5$		1
Semimajor axis (AU)	$1.84^{+0.04}_{-0.03}$		1
$M_{\text{tot}}$ ( $M_{\text{Jup}}$ )	$88 \pm 5$		1
$q \equiv M_B/M_A$	$0.78 \pm 0.07$		1
Mass ( $M_{\text{Jup}}$ )	$49 \pm 3$	$39 \pm 3$	1,2
Spectral type	L6.5 $\pm$ 1.5	T1.5 $\pm$ 1.0	1
$J$ (mag)	$16.89 \pm 0.06$	$16.44 \pm 0.05$	1,2
$H$ (mag)	$15.81 \pm 0.05$	$15.87 \pm 0.05$	1,2
$K$ (mag)	$14.99 \pm 0.04$	$15.50 \pm 0.04$	1,2
$J - H$ (mag)	$1.08 \pm 0.08$	$0.57 \pm 0.07$	1,2
$H - K$ (mag)	$0.82 \pm 0.06$	$0.37 \pm 0.06$	1,2
$J - K$ (mag)	$1.90 \pm 0.07$	$0.94 \pm 0.06$	1,2
$M_J$ (mag)	$14.81 \pm 0.07$	$14.36 \pm 0.06$	1,2
$M_H$ (mag)	$13.73 \pm 0.06$	$13.79 \pm 0.06$	1,2
$M_K$ (mag)	$12.90 \pm 0.05$	$13.42 \pm 0.06$	1,2
$BC_K$ (mag)	$3.25 \pm 0.10$	$2.91 \pm 0.13$	1,3
$\log(L_{\text{bol}}/L_{\odot})$	$-4.56 \pm 0.05$	$-4.63 \pm 0.06$	1
$\Delta \log(L_{\text{bol}})$	$0.07 \pm 0.07$		1
Parallax (mas)	$38.4 \pm 0.7$		1
$\mu_{\text{R.A.}}$ (mas yr $^{-1}$ )	$+19 \pm 3$		1
$\mu_{\text{Dec.}}$ (mas yr $^{-1}$ )	$-140 \pm 3$		1

Note. — All near-infrared photometry is on the MKO system. Parallax and proper motion have the following additive offsets applied to correct for the mean motion of our astrometric reference grid:  $\Delta\pi = 1.7 \pm 0.3$  mas,  $\Delta\mu_{\text{R.A.}} = -6 \pm 3$  mas yr $^{-1}$ ,  $\Delta\mu_{\text{Dec.}} = -7 \pm 3$  mas yr $^{-1}$ .

References. — (1) This work; (2) Chiu et al. (2006); (3) Liu et al. (2010).

Table 5. Evolutionary model-derived properties for SDSS J1052+4422AB

Property	Saumon & Marley (2008) hybrid			SM08 cloudy ( $f_{\text{sed}} = 2$ )			Lyon Dusty (Chabrier et al. 2000)		
	Median	68.3% c.i.	95.4% c.i.	Median	68.3% c.i.	95.4% c.i.	Median	68.3% c.i.	95.4% c.i.
Using individual masses and luminosities									
$t_A$ (Gyr)	1.22	0.99, 1.43	0.82, 1.69	0.95	0.79, 1.07	0.69, 1.30	1.01	0.84, 1.16	0.72, 1.36
$t_B$ (Gyr)	0.99	0.79, 1.17	0.63, 1.39	0.66	0.55, 0.77	0.45, 0.90	0.66	0.54, 0.76	0.45, 0.90
$\log(t_A/\text{yr})$	9.09	9.01, 9.17	8.93, 9.24	8.98	8.91, 9.04	8.86, 9.12	9.01	8.94, 9.08	8.87, 9.14
$\log(t_B/\text{yr})$	9.00	8.92, 9.09	8.82, 9.16	8.82	8.75, 8.89	8.67, 8.96	8.82	8.74, 8.89	8.67, 8.97
$\Delta \log t$ (dex)	0.09	-0.03, 0.21	-0.15, 0.33	0.16	0.06, 0.26	-0.03, 0.36	0.19	0.09, 0.29	-0.01, 0.39
$T_{\text{eff,A}}$ (K)	1340	1310, 1370	1280, 1400	1320	1280, 1360	1250, 1400	1360	1320, 1390	1280, 1430
$T_{\text{eff,B}}$ (K)	1270	1230, 1300	1200, 1330	1240	1190, 1270	1160, 1320	1260	1220, 1300	1180, 1340
$\Delta T_{\text{eff}}$ (K)	70	30, 110	-10, 150	90	40, 140	-10, 180	100	50, 150	0, 190
$\log(g_A)$ (cgs)	5.14	5.10, 5.18	5.05, 5.22	5.12	5.07, 5.16	5.03, 5.21	5.15	5.10, 5.20	5.05, 5.24
$\log(g_B)$ (cgs)	5.00	4.96, 5.05	4.92, 5.09	4.96	4.91, 5.01	4.86, 5.05	4.99	4.94, 5.03	4.89, 5.08
$R_A$ ( $R_{\text{Jup}}$ )	0.947	0.929, 0.965	0.912, 0.983	0.970	0.953, 0.987	0.934, 1.004	0.939	0.923, 0.957	0.901, 0.973
$R_B$ ( $R_{\text{Jup}}$ )	0.972	0.950, 0.991	0.934, 1.017	1.023	1.003, 1.041	0.985, 1.063	0.991	0.972, 1.010	0.955, 1.030
(Li/Li <sub>0</sub> ) <sub>A</sub>	...	...	...	...	...	...	0.947	0.930, 0.986	0.545, 1.000
(Li/Li <sub>0</sub> ) <sub>B</sub>	...	...	...	...	...	...	1.0	1.0, 1.0	1.0, 1.0
$(Y - J)_A$ (mag)	1.205	1.200, 1.212	1.187, 1.214	1.201	1.194, 1.212	1.176, 1.215	...	...	...
$(Y - J)_B$ (mag)	1.182	1.165, 1.206	1.134, 1.215	1.16	1.13, 1.18	1.12, 1.21	...	...	...
$(J - H)_A$ (mag)	1.04	0.94, 1.14	0.86, 1.21	0.98	0.90, 1.13	0.71, 1.16	2.51	2.41, 2.61	2.31, 2.71
$(J - H)_B$ (mag)	0.73	0.57, 0.91	0.37, 1.02	0.55	0.32, 0.69	0.26, 0.92	2.78	2.68, 2.90	2.56, 3.00
$(H - K)_A$ (mag)	0.71	0.56, 0.87	0.44, 0.99	0.62	0.48, 0.87	0.26, 0.94	2.05	1.96, 2.15	1.85, 2.25
$(H - K)_B$ (mag)	0.29	0.09, 0.50	-0.12, 0.65	0.09	-0.17, 0.22	-0.18, 0.53	2.33	2.26, 2.42	2.14, 2.48
$(J - K)_A$ (mag)	1.8	1.5, 2.0	1.3, 2.2	1.6	1.4, 2.0	1.0, 2.1	4.56	4.36, 4.75	4.16, 4.96
$(J - K)_B$ (mag)	1.0	0.7, 1.4	0.2, 1.7	0.6	0.1, 0.9	0.1, 1.5	5.11	4.93, 5.32	4.69, 5.48
$(K - L')_A$ (mag)	1.25	1.21, 1.29	1.18, 1.34	1.28	1.22, 1.32	1.18, 1.39	1.92	1.82, 2.03	1.72, 2.13
$(K - L')_B$ (mag)	1.36	1.29, 1.42	1.25, 1.50	1.42	1.35, 1.50	1.28, 1.57	2.23	2.12, 2.35	1.98, 2.44



Table 5—Continued

Property	Saumon & Marley (2008) hybrid			SM08 cloudy ( $f_{\text{sed}} = 2$ )			Lyon Dusty (Chabrier et al. 2000)		
	Median	68.3% c.i.	95.4% c.i.	Median	68.3% c.i.	95.4% c.i.	Median	68.3% c.i.	95.4% c.i.
Using total mass, individual luminosities, and assuming coevality									
Age ( $t$ , Gyr)	1.11	0.91, 1.28	0.76, 1.49	0.81	0.69, 0.91	0.60, 1.04	0.84	0.69, 0.94	0.61, 1.09
$\log(t/\text{yr})$	9.04	8.97, 9.12	8.89, 9.18	8.91	8.85, 8.97	8.79, 9.02	8.92	8.86, 8.99	8.79, 9.05
$M_{\text{A}}$ ( $M_{\text{Jup}}$ )	47	43, 51	40, 55	45.8	42.8, 48.6	40.3, 51.7	45.5	42.6, 48.2	40.0, 51.5
$M_{\text{B}}$ ( $M_{\text{Jup}}$ )	41	38, 44	35, 48	42.6	39.7, 45.2	37.5, 48.4	43.1	40.4, 45.9	37.6, 48.7
$q \equiv M_{\text{B}}/M_{\text{A}}$	0.87	0.78, 0.98	0.67, 1.09	0.93	0.87, 0.98	0.83, 1.06	0.94	0.89, 0.99	0.85, 1.05
$T_{\text{eff,A}}$ (K)	1330	1300, 1360	1270, 1400	1310	1270, 1340	1240, 1380	1340	1300, 1370	1270, 1410
$T_{\text{eff,B}}$ (K)	1270	1240, 1310	1200, 1350	1250	1210, 1290	1170, 1340	1280	1230, 1320	1200, 1370
$\Delta T_{\text{eff}}$ (K)	60	0, 100	−50, 160	60	20, 120	−50, 160	60	10, 120	−50, 170
$\log(g_{\text{A}})$ (cgs)	5.10	5.06, 5.15	5.01, 5.19	5.06	5.02, 5.10	4.98, 5.14	5.09	5.04, 5.13	5.00, 5.18
$\log(g_{\text{B}})$ (cgs)	5.04	5.00, 5.09	4.95, 5.13	5.03	4.98, 5.06	4.95, 5.11	5.06	5.02, 5.10	4.97, 5.14
$R_{\text{A}}$ ( $R_{\text{Jup}}$ )	0.958	0.940, 0.974	0.924, 0.993	0.991	0.975, 1.007	0.959, 1.022	0.958	0.939, 0.969	0.930, 0.993
$R_{\text{B}}$ ( $R_{\text{Jup}}$ )	0.960	0.942, 0.977	0.927, 0.997	0.998	0.983, 1.013	0.967, 1.027	0.963	0.944, 0.975	0.934, 0.997
(Li/Li <sub>0</sub> ) <sub>A</sub>	...	...	...	...	...	...	0.977	0.968, 1.000	0.943, 1.000
(Li/Li <sub>0</sub> ) <sub>B</sub>	...	...	...	...	...	...	0.992	0.984, 1.000	0.960, 1.000
$(Y - J)_{\text{A}}$ (mag)	1.205	1.200, 1.213	1.185, 1.215	1.200	1.191, 1.214	1.171, 1.216	...	...	...
$(Y - J)_{\text{B}}$ (mag)	1.184	1.167, 1.206	1.138, 1.214	1.17	1.14, 1.19	1.12, 1.21	...	...	...
$(J - H)_{\text{A}}$ (mag)	1.01	0.90, 1.13	0.80, 1.20	0.92	0.81, 1.08	0.65, 1.14	2.57	2.47, 2.67	2.37, 2.76
$(J - H)_{\text{B}}$ (mag)	0.77	0.60, 0.95	0.38, 1.07	0.64	0.40, 0.81	0.29, 1.01	2.73	2.62, 2.85	2.48, 2.96
$(H - K)_{\text{A}}$ (mag)	0.67	0.48, 0.83	0.38, 0.98	0.54	0.36, 0.73	0.18, 0.89	2.10	2.01, 2.20	1.91, 2.29
$(H - K)_{\text{B}}$ (mag)	0.3	0.1, 0.6	−0.1, 0.7	0.18	−0.10, 0.37	−0.17, 0.65	2.26	2.16, 2.36	2.03, 2.44
$(J - K)_{\text{A}}$ (mag)	1.7	1.4, 2.0	1.2, 2.2	1.5	1.2, 1.8	0.8, 2.0	4.67	4.48, 4.87	4.28, 5.03
$(J - K)_{\text{B}}$ (mag)	1.1	0.7, 1.5	0.3, 1.8	0.8	0.3, 1.2	0.1, 1.7	5.0	4.8, 5.2	4.5, 5.4
$(K - L')_{\text{A}}$ (mag)	1.26	1.22, 1.30	1.18, 1.35	1.29	1.24, 1.34	1.20, 1.40	1.99	1.89, 2.09	1.78, 2.18
$(K - L')_{\text{B}}$ (mag)	1.35	1.28, 1.41	1.23, 1.50	1.40	1.33, 1.49	1.25, 1.55	2.16	2.04, 2.27	1.91, 2.37

|  
Σ  
|

